Auxiliary material for

Carbon export by small particles in the Norwegian Sea

Giorgio Dall'Olmo[1,2] and Kjell Arne Mork[3,4]

1, Plymouth Marine Laboratory, Plymouth, UK.

2, National Centre for Earth Observation, UK.

3, Institute for Marine Research, Bergen, Norway.

4, Centre for Climate Dynamics, Bergen, Norway.

Geophysical Research Letters

Additional description of the measurements

1. The WETLabs ECO-FLBB instruments were programmed to sample for approximately 1 second at prescribed pressures with vertical resolution increasing towards the surface (i.e., every 25 m between 1000 and 500 m, every 20 m between 500 and 400 m, every 10 m between 400 and 150 m, and every 5 m between 150 and 5 m).
2. The floats were originally equipped with SBE oxygen sensors, but these failed shortly after deployments and are thus not available for this analysis.

Argument supporting the sensing of small particles

The arguments below are provided in support of the statement that low-pass filtered particulate optical backscattering (b_{bp}) data are sensitive to small particles.

1. Particles larger than about 20um should appear as spikes in b_{bp} measurements [Briggs et al., 2013]. We used a median filter to remove most/all spikes from our datasets [see Figure 2].
2. In addition, the influence of large particles was further reduced in our measurements, because relatively large volumes of water were sampled by the b_{bp} instruments. The volume of water sampled by each measurement was about 10-30 times larger than the volume the instrument would have sampled if the float had not been not moving vertically. The work by Briggs et al. [2013] can be used to predict how optical spikes due to large particles affected our b_{bp} measurements. Sample volume is inversely related to the variance-to-mean ratio (which increases when the concentration of large particles increases) of the measured optical property [eq. A6 in Briggs et al., 2013]. Thus, the b_{bp} values recorded when the floats were ascending are expected to be less affected by spikes generated by large particles. This is because, although there are in average more large particles in a larger volume of sampled water, the relevant quantity affecting optical measurements is

their concentration. Large particles are very rare in a small volume of water. When they do occur, however, their concentration is significantly larger than in a larger volume of water and the optical instrument records a spike. In summary, binning optical data (or sampling when the instrument is moving with respect to the water) increases the volume of water sampled and decreases the influence of spikes, without increasing significantly the mean value of the measured optical property [eq. 14 in Briggs et al., 2013].

3. Simulations based on particle size distributions measured in the upper productive layer (and thus more abundant in large particles than deeper layers), suggest that, to first order, a dominant (>95%) fraction of b_{bp} is generated by particles smaller than 10um [Stramski and Kiefer, 1991; Morel and Ahn, 1991]. Although the complexity of marine particles may invalidate the results of the above simulations, these modeling results nevertheless support, at least to first order, the statement that b_{bp} signals are generated by small particles.

In summary, although we do not have direct observations of the sampled particles (besides our optical measurements), based on the above arguments, we conclude that it is highly unlikely that the smoothed b_{bp} values presented in this manuscript were generated by particles greater than about 10-20um. Most likely, particles smaller than 10um contributed the majority of the b_{bp} signal.

Uncertainty estimation for instantaneous fluxes and transfer efficiencies

Uncertainties in instantaneous fluxes and transfer efficiencies were computed following a Monte Carlo approach. The uncertainties in these output variables were assumed to be due to uncertainties in the input parameters required for their computation: (1) the b_{bp} values, and the POC:b_{bp} ratios (2) within and (3) below the mixed layer. Independent normally-distributed random distributions (N=1000 for each input variable) were generated using as averages the measured b_{bp} values at each point sampled by each float and the POC:b_{bp} values from Cetinic et al., (2012, the averages of the two communities within and below the mixed layer). The uncertainties (i.e., standard deviations) associated with each input variable were computed as follows. The combined experimental uncertainty in b_{bp} was estimated following Dall'Olmo et al. (2012) by accounting for the uncertainties in the scaling factors (S), chi-factor (χ_p) and instrument precision (C; Table A1). The symbols are provided to facilitate a comparison with Table 3 in Dall'Olmo et al. (2012). Note that uncertainties in dark counts (D) and the volume scattering function of pure sea water (β_{sw}) were not included, because they represent biases that were removed by subtracting the minimum b_{bp} value from each time series (see Methods section).

Input variable	Uncertainty [units]
S	10%
χ_p	2.9%
C	2 [counts]

Table A1: Uncertainties in b_{bp} input variables.

The uncertainties in the POC:b_{bp} averages were conservatively estimated as three times the squared root of the sum of the squared standard deviations reported for the two communities within and below the mixed layer by Cetinic et al. (2012). The resulting uncertainties in the POC:b_{bp} ratios within and below the mixed layer were: 8475 and 6282 mg C m^2, respectively.

An example of the Monte Carlo output is presented in Figure A1. Furthermore, to provide an overall picture of the impact of noise (uncertainties) on our estimates, we present in Figure A2 the signal-to-noise ratios (SNR) of our instantaneous flux estimates. These SNR were computed as the ratio of the mean to the standard deviation of the 1000 Monte Carlo realizations. Figure A2 demonstrates that the SNR was typically above 1 and reached values greater than 4 when fluxes were maximal.

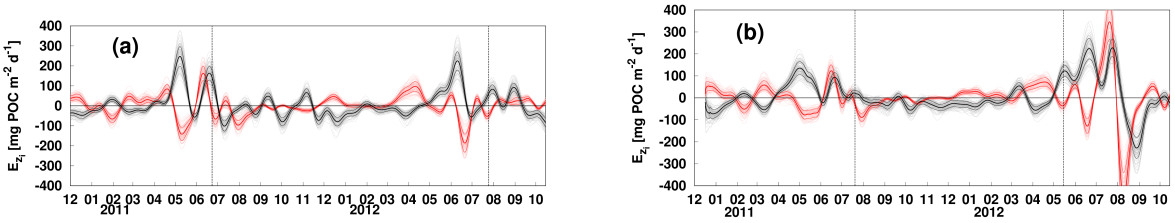

Figure A1: Example of the Monte Carlo output for E_{zp} (thin pink lines) and E_0 (thin gray lines). The averages (+/- 1 standard deviation) are also presented as thicker lines. (a) Float 6900798, (b) float 6900799.

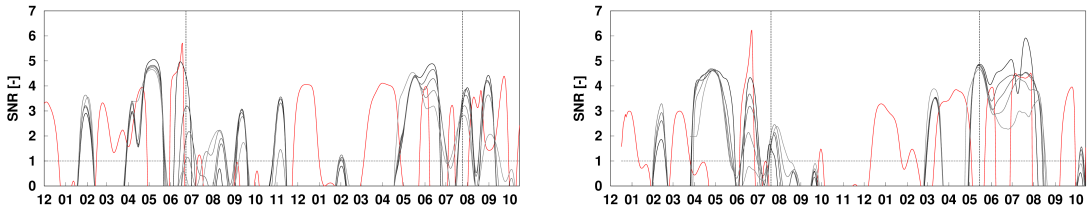

Figure A2: Signal-to-noise ratios (SNR) computed for each instantaneous flux. Colors and vertical dashed lines are as in Figure 3 of the main text. The horizontal dashed lines mark the SNR=1, when the standard deviation equals the mean of the 1000 Monte Carlo realizations. (a) Float 6900798, (b) float 6900799.

Uncertainties in *E* and spatial-homogeneity requirements in the open ocean

In this section we derive an analytical approximation to estimate the uncertainty in the export flux. We then use this approximation to estimate the uncertainty in flux that is obtained when integrating float-based measurements over a given amount of time.

The flux *E* within a given layer of the mesopelagic is here defined as the rate of change of *iPOC* during a period of time ($\Delta t = t_2 - t_1$):

$$E = \frac{\Delta\, iPOC}{\Delta t} = \frac{\Delta P}{\Delta t} = \frac{P_2 - P_1}{t_2 - t_1}$$, where P_i stands for $iPOC_i$.

The variance in *E* is thus (standard law of propagation of uncertainties):

$$\sigma_E^2 = \left(\frac{\partial \Delta P}{\partial P_2}\sigma_{P2}\right)^2 + \left(\frac{\partial \Delta P}{\partial P_1}\sigma_{P1}\right)^2 + 2\frac{\partial \Delta P}{\partial P_1}\frac{\partial \Delta P}{\partial P_2}\sigma_{P1}\sigma_{P2}\rho_{12} \quad ,$$

where σ_{P1}, σ_{P2} and ρ_{12} are the uncertainties in P_1 and P_2 and the correlation coefficient between P_1 and P_2, respectively.

Thus, in general:

$$\sigma_E^2 = \frac{\sigma_{iPOC2}^2 + \sigma_{iPOC1}^2 - 2\sigma_{iPOC1}\sigma_{iPOC2}\rho_{12}(\Delta t)}{\Delta t^2} \qquad (1).$$

Here we assume that the *relative* error in *iPOC*, σ_r, is approximately constant, consistent with the results from our Monte Carlo calculations when the water column is stratified (see Table A2 below). In addition, we assume that time *t* has no uncertainties and that *iPOC* grows linearly with time, which allows us to set a fixed value for *E* (as a first approximation). Then,

$$P_2 = E\Delta t + P_1 \qquad (2).$$

By combining equations (1) and (2) the (squared) relative error in *E* can be obtained:

$$\frac{\sigma_E^2}{E^2} = \sigma_r^2\frac{P_2^2 + P_1^2 - 2P_1P_2\rho}{E^2\Delta t^2} = \sigma_r^2\frac{(E\Delta t + P_1)^2 + P_1^2 - 2P_1(E\Delta t + P_1)\rho}{E^2\Delta t^2} \quad .$$

We can then derive an expression that allows us to estimate the (squared) ratio of the relative error in *E* as a function of the (squared) relative error in *iPOC* (which is known) and of Δt:

$$\sigma = 1 + 2\frac{P_1}{E\Delta t}(1-\rho) + 2\left(\frac{P_1}{E\Delta t}\right)^2(1-\rho) \qquad (3),$$

where $\sigma = [(\sigma_E/E)/\sigma_r]^2$, *and* ρ is the autocorrelation function.

Equation (3) allows us to understand how fast the relative error in *E* approaches its minimum value as Δt increases.

The limit results are:

a) *as* $E\Delta t \rightarrow 0$, $\sigma_E{:}E \rightarrow +\infty$
b) as $E\Delta t \rightarrow +\infty$, $\sigma_E{:}E \rightarrow \sigma_r$,
c) as $P_1 \rightarrow 0$, $\sigma_E{:}E \rightarrow \sigma_r$,
d) as $P_1 \rightarrow +\infty$, $\sigma_E{:}E \rightarrow +\infty$.
e) if $\rho=1$, *then* $\sigma_E{:}E = \min(\sigma_E{:}E) = \sigma_r$.

Thus, according to equation (3), the relative uncertainty in *E* ($\sigma_E{:}E$) can never be smaller than the relative

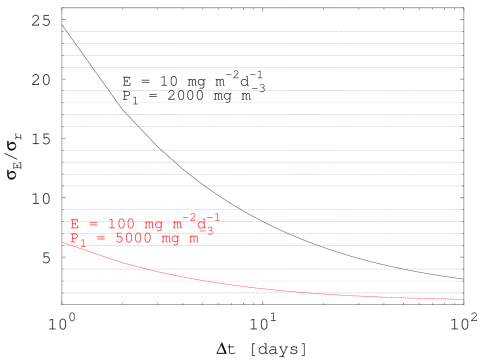

Figure A3: Ratio of relative error in E to relative error in iPOC as a function of Δt, for two values of E and corresponding typical values of iPOC. Low export case: E = 10 mg m^{-2} d^{-1}; P_1 = 2000 mg m^{-3}. High export case: E = 100 mg m^{-2} d^{-1}; P_1= 5000 mg m^{-3}.

uncertainty in *iPOC* (σ_r). This minimum error is achieved for very large integration times (i.e., Δt).

Figure A3 is a plot of σ computed using equation (3) and accounting for the autocorrelation as a function of Δt. (The autocorrelation of our raw *iPOC* dataset varied approximately linearly between 1 and 0.25 for Δt = [1:100], independent of depth).

Typical *iPOC* relative errors ranged between about 20% and 60% during the stratified period, with maximal values found in winter and typical (mean±st.dev.) values between spring and autumn as in Table A2.

Extremes of depth integration	**Float 6900798**	**Float 6900799**
0; zp	0.217 ± 0.019	0.219 ± 0.019
zp; 1000	0.204 ± 0.006	0.204 ± 0.006
zp+100; 1000	0.214 ± 0.003	0.214 ± 0.004
zp+200; 1000	0.219 ± 0.004	0.219 ± 0.005
zp+300; 1000	0.226 ± 0.006	0.227 ± 0.006
zp+400; 1000	0.237 ± 0.007	0.237 ± 0.007
zp+500; 1000	0.249 ± 0.008	0.249 ± 0.008

Table A2: Average and standard deviations of typical iPOC uncertainties between spring and summer.

Table A3 presents typical uncertainties in E_{zi} resulting for integration times of 10 and 30 days for the low and high export cases of Figure A3 and for the average errors reported in Table A2.

Extremes of depth integration	**Integration time = 10 days**		**Integration time = 30 days**	
	Low export	**High export**	**Low export**	**High export**
0; zp	1.75	1.07	0.51	0.38
zp; 1000	1.63	1.00	0.48	0.35
zp+100; 1000	1.71	1.05	0.50	0.37
zp+200; 1000	1.75	1.07	0.51	0.38
zp+300; 1000	1.81	1.11	0.53	0.39
zp+400; 1000	1.90	1.16	0.56	0.41
zp+500; 1000	1.99	1.22	0.58	0.43

Table A3: Uncertainties in E_{zi} computed using Eq. (3) and obtained from uncertain iPOC estimates taken 10 and 30 days apart for the two export scenarios described in Figure A3.

Thus, for a high-export case (E = 100 mg m^{-2} d^{-1}), we expect a typical relative uncertainty

in E ranging from 35% to 43%, when using a Δt =30 days. Uncertainties increase when E decreases to 10 mg m^{-2} d^{-1} or when Δt decreases.

If a float drifts at depth in a straight line at an average speed of 5.4 cm/s [Ollitrault and Rannou, 2013], over 30 days it will have traveled about 140 km. Therefore, assuming that the uncertainties in POC:b_{bp} are realistic, to compute export over regions where the floats are not confined in a given basin, an assumption of spatial homogeneity over typical scales of 150 km is required. Improved estimates of the POC:b_{bp} ratio would significantly reduce uncertainties and allow to relax the above assumption.

Additional plots

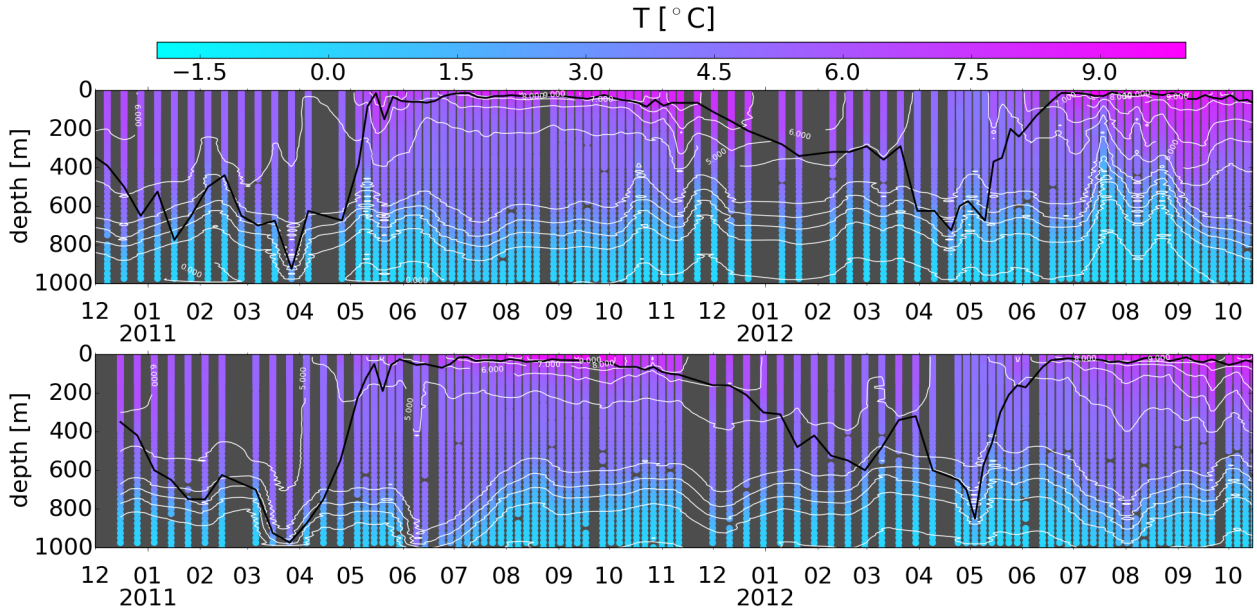

Figure A4: Temperature data (colors and white contours) for floats 6900798 (top) and 6900799 (bottom). The black line is the mixed layer depth estimate based on the 0.10 kg m^{-3} density criterion.

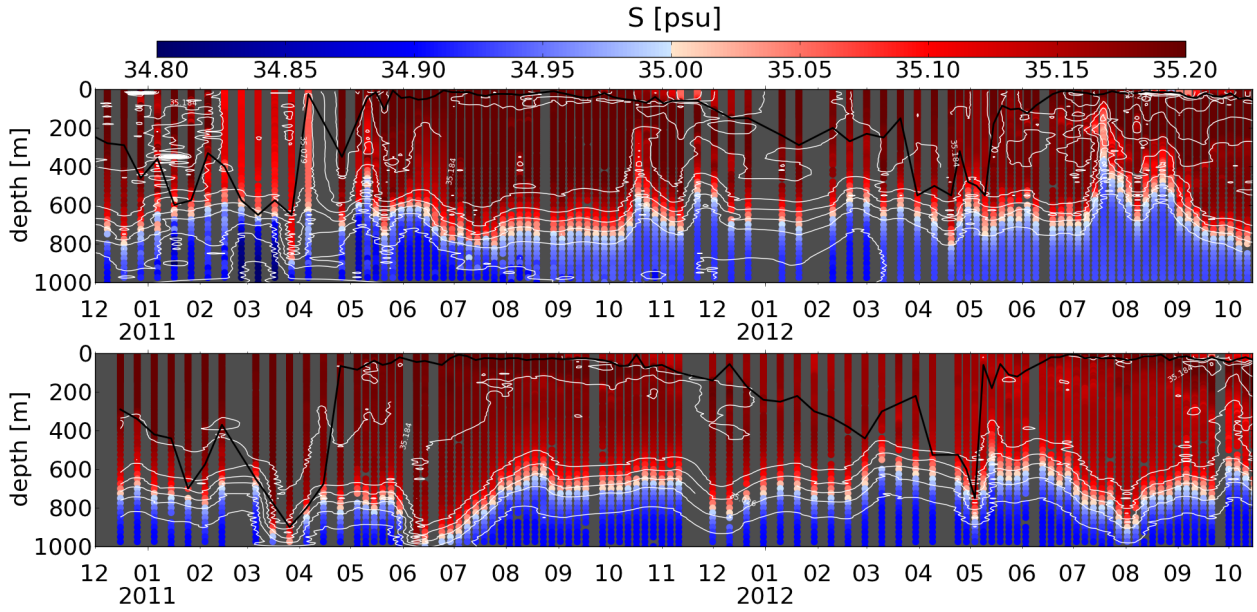

Figure A5: Salinity data (colors and white contours) for floats 6900798 (top) and 6900799 (bottom). The black line is the mixed-layer-depth estimate based on the 0.10 kg m^{-3} density criterion. Red and blue colors have been selected to differentiate the two main water masses of the region: (red) the saltier and warmer Atlantic Water, and (blue) the cooler and fresher Arctic Water.

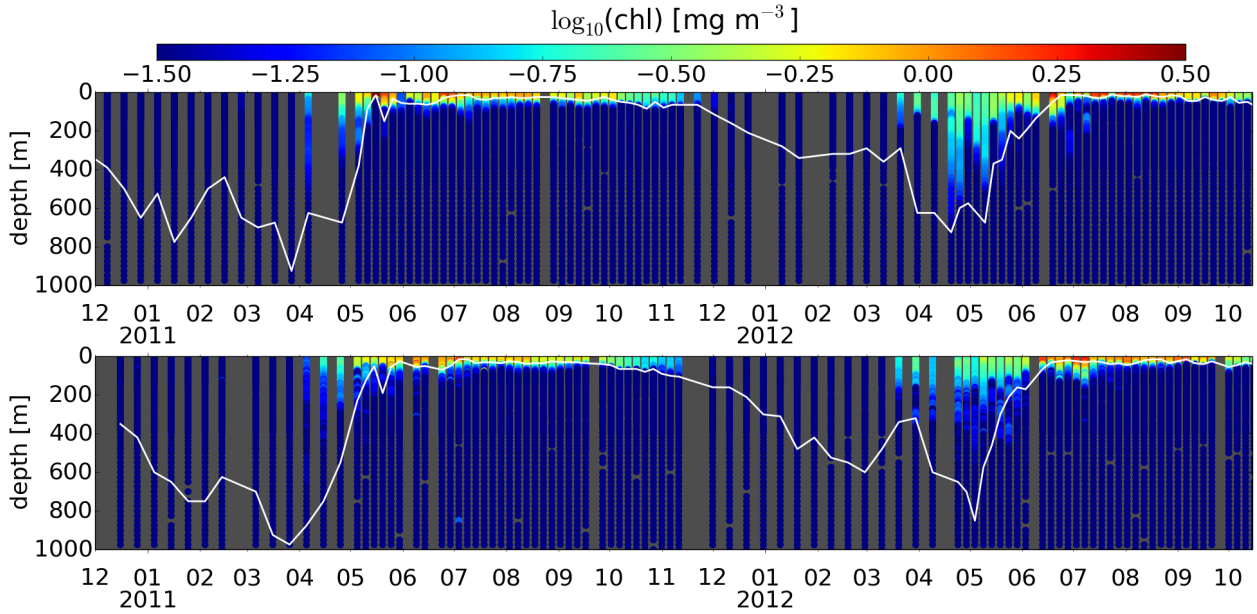

Figure A6: Chlorophyll fluoresce data for floats 6900798 (top) and 6900799 (bottom). White lines are mixed-layer-depth estimates based on the 0.10 kg m^{-3} density criterion.

MODIS estimates of Particulate Inorganic Carbon

Particulate Inorganic Carbon (PIC) estimates were obtained from NASA Giovanni for 2011 and 2012. Figure A7 demonstrates that in 2012 elevated concentrations of PIC were found in the region sampled by the floats (70degN, 0-5degE).

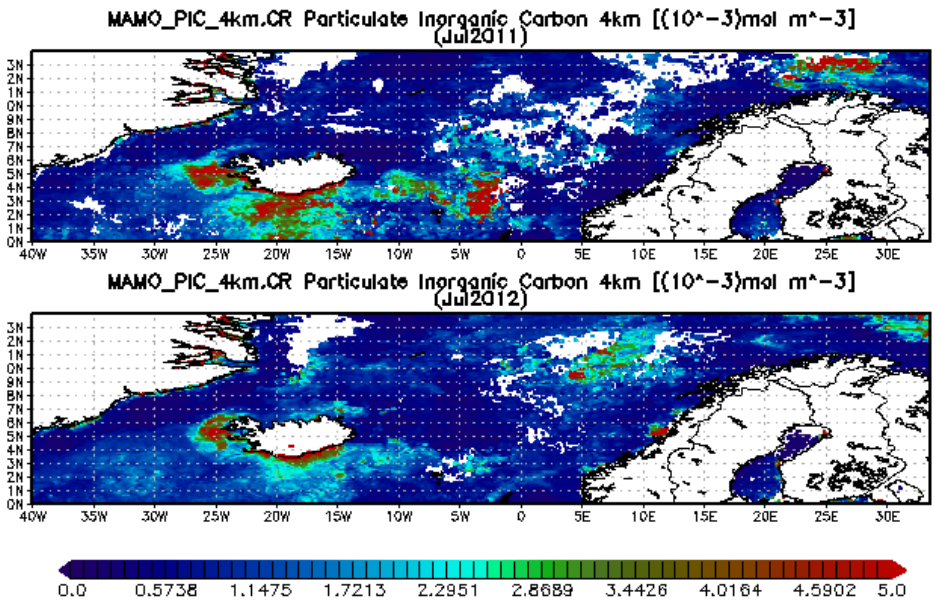

Figure A7: NASA Giovanni images of MODIS estimates of particulate inorganic carbon from 2011 and 2012. White areas are land or clouds.

Estimation of euphotic depth

The depth of the bottom of the euphotic zone (z_{eu}, i.e., 1% of surface irradiance) was computed based on an empirical relationship (Figure A7) that was established between float-based surface (10 m) *chl* and MODIS AQUA remote-sensing estimates of z_{eu}:

$(z_{eu})^{-1} = 0.012939 + 0.018151\ chl_{10}$.

The R^2 of the log-transformed relationship was 0.70.

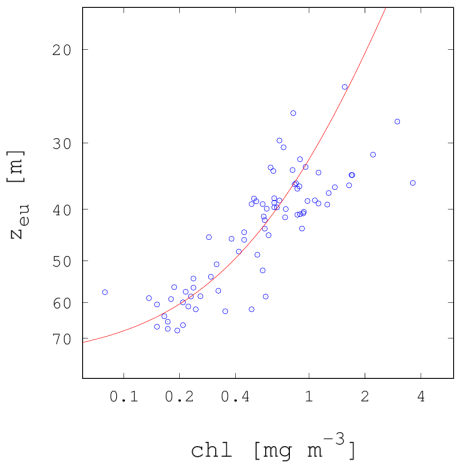

Figure A8: Empirical fit relating MODIS estimates of z_{eu} and float-based measurements of chl fluorescence at a depth of 10 m.

References

Briggs, N. T.; Slade, W. H.; Boss, E. & Perry, M. J. Method for estimating mean particle size from high-frequency fluctuations in beam attenuation or scattering measurements. *Appl. Opt., Applied Optics, OSA,* **2013***, 52*, 6710-6725.

Cetinic, I.; Perry, M. J.; Briggs, N. T.; Kallin, E.; D'Asaro, E. A. & Lee, C. M. Particulate organic carbon and inherent optical properties during 2008 North Atlantic Bloom Experiment. *J. Geophys. Res., AGU,* **2012***, 117*, C06028.

Dall'Olmo, G.; Boss, E.; Behrenfeld, M. & Westberry, T. Particulate optical scattering coefficients along an Atlantic Meridional Transect. *Opt. Express, OSA,* **2012***, 20*, 21532-21551.

Kitchen, J. C. & Zaneveld, J. R. V. A three-layered sphere model of the optical properties of phytoplankton. *Limnology and Oceanography,* **1992***, 37*, 1680-1690.

Meyer, R. A. Light-scattering from biological cells - Dependence of backscatter radiation on membrane thickness and refractive-index. *Applied Optics, Optical Soc Amer,* **1979***, 18*, 585-588.

Morel, A. & Ahn, Y. H. Optics of heterotrophic nanoflagellates and ciliates - a tentative assessment of their scattering role in oceanic waters compared to those of bacterial and algal cells. *Journal of Marine Research,* **1991***, 49*, 177-202.

Ollitrault, M. & Rannou, J. P. ANDRO: An Argo-Based Deep Displacement Dataset *Journal of Atmospheric and Oceanic Technology,* **2013***, 30*, 759-788.

Stramski, D. & Kiefer, D. Light scattering by microorganisms in the open ocean *Progress in Oceanography,* **1991***, 28*, 343-383.